deviation of the background according to previous reports (17,22). These ROIs were selected for the following reasons: middle cerebellar peduncle for white matter in the posterior fossa; globus pallidus for magnetic susceptibility induced by ferritin; and centrum semiovale and splenium for white matter in the supratentorial region. SNR index was determined as SNR at 3 T divided by SNR at 1.5 T.

Statistical analysis

JMP 5.1 (SAS Institute Inc., Cary, NC, USA) was used for statistical analysis. A paired *t* test was performed on the following histogram data at both 3 T and 1.5 T: peak location; peak height; mean FA; mean MD; normalized voxels for each bin of FA and MD. For the MD histogram, any bin containing <0.5% of normalized voxels was considered as noise and excluded from statistical analysis. A paired *t* test was also applied for each value of ROI for FA and MD at both 3 T and 1.5 T. $P < 0.05$ was considered statistically significant.

RESULTS

Histogram analysis

Representative FA and MD images at both 3 T and 1.5 T are shown in Fig. 2. The results of FA histogram analysis are shown in Table 1. Peak location of FA was significantly lower at 3 T than at 1.5 T ($P = 0.04$). Mean FA was significantly higher at 3 T than at 1.5 T ($P = 0.002$). The results of MD histogram analysis are shown in Table 2. Peak location of MD was significantly lower at 3 T than at 1.5 T imaging ($P < 0.001$). Mean MD was significantly lower at 3 T than at 1.5 T ($P < 0.001$). The mean FA and MD histograms on which all the data were averaged by each bin are shown in Figs 3 and 4, respectively. These were different from individual histograms, and the information on peak locations and peak heights were compensated; however, they represent gross characteristics of FA and MD at 3 T and 1.5 T.

ROI analysis

FA was significantly larger at 3 T than at 1.5 T in the centrum semiovale ($P < 0.001$), middle cerebellar peduncle ($P < 0.001$), cerebral peduncle ($P = 0.006$), posterior limb of the internal capsule ($P = 0.007$), genu ($P < 0.001$) and splenium ($P < 0.001$) (Table 3). It was significantly smaller at 3 T than at 1.5 T in the globus pallidus ($P < 0.001$). MD was significantly smaller at 3 T than at 1.5 T in the globus pallidus ($P = 0.007$), thalamus ($P < 0.001$), centrum semiovale ($P < 0.001$), middle cerebellar peduncle ($P < 0.001$), cerebral peduncle

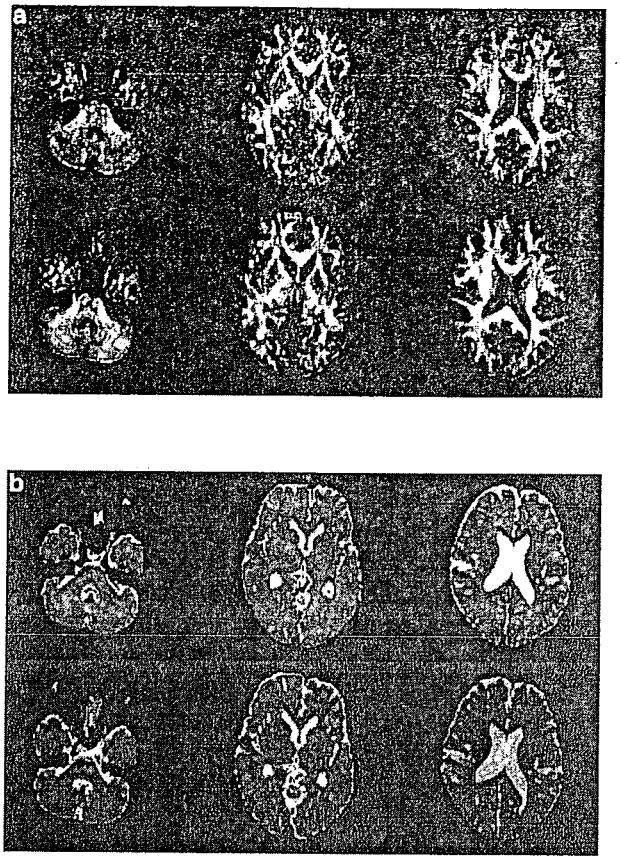

Figure 2. Transverse single-shot spin-echo echo-planar diffusion-tensor MRI at 3 T (*TR* 5200 ms, *TE* 79 ms) and 1.5 T (*TR* 5200 ms, *TE* 79 ms). (a) Top row shows images of FA obtained at 1.5 T. Bottom row shows images of FA obtained at 3 T. (b) Top row shows images of MD obtained at 1.5 T. Bottom row shows images of MD obtained at 3 T

Table 1. Histogram analysis for FA. Values are mean ± SD[Q3]

	1.5 T	3 T	*P* value
Peak location	0.111 ± 0.010	0.106 ± 0.013	0.04
Peak height (%)*	3.660 ± 0.129	3.681 ± 0.205	0.49
Mean FA	0.248 ± 0.007	0.253 ± 0.010	0.002

*Peak height for each volunteer was divided by the number of whole-brain voxels for normalization, therefore the data are percentages.

($P = 0.01$), posterior limb of the internal capsule ($P < 0.001$), genu ($P = 0.01$) and splenium ($P < 0.001$) (Table 4).

Table 5 shows SNR index values. All were larger than 1, including that for the middle cerebellar peduncle for the posterior fossa.

DISCUSSION

Several comparison studies of DTI at 1.5 T have been reported (23,24), but few have focused on the differences

Copyright © 2007 John Wiley & Sons, Ltd.

Table 2. Histogram analysis for MD. Values are mean ± SD

	1.5 T	3 T	*P* value
Peak location ($10^{-3} \times mm^2/s$)	0.862 ± 0.027	0.833 ± 0.025	<0.001
Peak height (%)*	8.094 ± 0.773	7.883 ± 1.176	0.102
Mean MD ($10^{-3} \times mm^2/s$)	1.019 ± 0.040	0.974 ± 0.041	<0.001

*Peak height for each volunteer was divided by the number of whole-brain voxels for normalization, therefore the data are percentages.

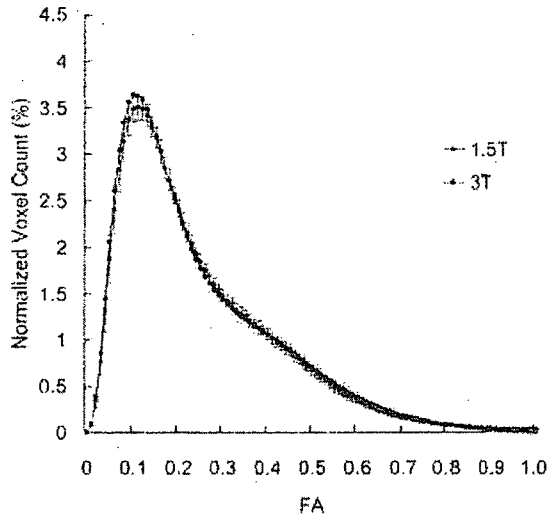

Figure 3. Mean histograms of FA at 3 T and 1.5 T. Error bars indicate standard deviations. Histograms were created for each FA image with a binwidth of 1% of maximum, and were divided by whole-brain voxels of that subject for normalization. The 3 T histogram is higher at both smaller value and larger values of FA than the 1.5 T histogram

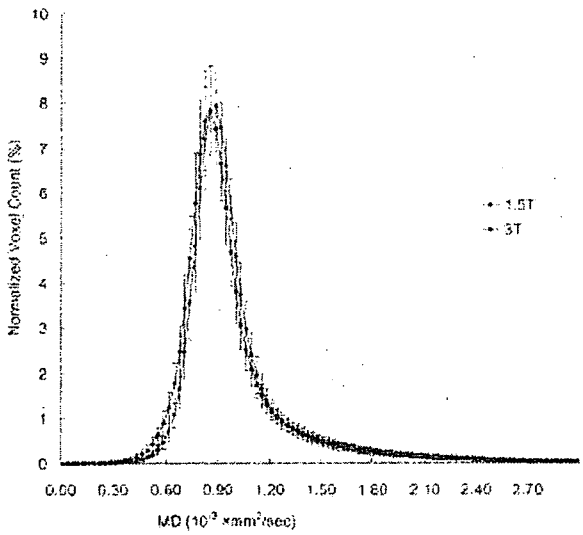

Figure 4. Mean histograms of MD at 3 T and 1.5 T. Error bars indicate standard deviations. Histograms were created for each MD image with a binwidth of 1% of maximum, and were divided by whole-brain voxels of that subject for normalization. The 3 T histogram shows a shift to the left

Table 3. ROI analysis of FA at 3 T and 1.5 T. Values are mean ± SD

	1.5 T	3 T	*P* value
GP	0.235 ± 0.039	0.197 ± 0.038	<0.001
Th	0.295 ± 0.032	0.286 ± 0.021	0.17
CS	0.477 ± 0.041	0.551 ± 0.040	<0.001
mCP	0.566 ± 0.058	0.615 ± 0.041	<0.001
CP	0.644 ± 0.067	0.682 ± 0.049	0.006
plC	0.682 ± 0.040	0.701 ± 0.037	0.007
genu	0.766 ± 0.052	0.821 ± 0.041	<0.001
splenium	0.799 ± 0.037	0.847 ± 0.033	<0.001

GP, Globus pallidus; Th, thalamus; CS, centrum semiovale; mCP, middle cerebellar peduncle; CP, cerebral peduncle; plC, posterior limb of the internal capsule.

Table 4. ROI analysis of MD at 3 T and 1.5 T. Values are mean ± SD

MD ($10^{-3} \times mm^2/s$)	1.5 T	3 T	*P* value
GP	0.863 ± 0.045	0.819 ± 0.063	0.007
Th	0.866 ± 0.027	0.800 ± 0.024	<0.001
CS	0.846 ± 0.026	0.776 ± 0.026	<0.001
mCP	0.845 ± 0.031	0.778 ± 0.027	<0.001
CP	0.905 ± 0.118	0.808 ± 0.139	0.01
plC	0.826 ± 0.027	0.785 ± 0.023	<0.001
Genu	0.863 ± 0.090	0.810 ± 0.065	0.01
Splenium	0.795 ± 0.049	0.717 ± 0.058	<0.001

GP, Globus pallidus; Th, thalamus; CS, centrum semiovale; mCP, middle cerebellar peduncle; CP, cerebral peduncle; plC, posterior limb of the internal capsule.

Table 5. SNR index of DTI. Values are mean ± SD

	SNR index
GP	1.40 ± 0.31
mCP	1.48 ± 0.29
CS	1.71 ± 0.38
genu	1.67 ± 0.48

SNR index was calculated as SNR at 3 T divided by SNR at 1.5 T. GP, Globus pallidus; CS, centrum semiovale; mCP, middle cerebellar peduncle.

between 3 T and 1.5 T (17,18). Hunsche *et al.* (17) reported differences in DTI among seven healthy volunteers at 3 T and 1.5 T using ROI analysis; however, the data were obtained with the conventional technique without using parallel imaging. There are no articles

Copyright © 2007 John Wiley & Sons, Ltd.

featuring the differences in recent DTI using parallel imaging between 3 T and 1.5 T. In our study, the differences in FA and MD at both magnets were evaluated by using histogram and ROI analyses.

Histogram analyses showed that mean FA at 3 T was significantly higher than at 1.5 T, and the peak location of FA was significantly lower at 3 T than at 1.5 T. In histograms, the peak of FA represents a smaller value of FA, i.e. less anisotropic tissue such as gray matter. Higher mean FA and lower peak location at 3 T may represent better contrast between the larger and smaller value of FA. ROI analysis of FA at 3 T showed a significantly larger value than at 1.5 T for the centrum semiovale, middle cerebellar peduncle, cerebral peduncle, posterior limb of the internal capsule, genu, and splenium. These ROIs indicate relatively anisotropic tissues. Our results may support better visualization of DT tractography at 3 T than at 1.5 T (17,18).

The MD histogram at 3 T showed significantly lower peak location and mean MD than at 1.5 T. ROI analyses also revealed that all the ROIs of MD at 3 T were smaller than at 1.5 T. Our results are consistent with a previous study (17). FA of the globus pallidus was significantly lower at 3 T than at 1.5 T, and this might be attributable to increased susceptibility at 3 T of ferritin in the globus pallidus.

The SNR for DTI at 3 T showed a 1.40 ± 0.31 to 1.70 ± 0.38 gain compared with that at 1.5 T. Hunsche *et al.* (17) reported a 1.4 ± 0.2 gain in white matter at 3 T using a standard head coil; however, they excluded infratentorial regions from the analysis. Gonen *et al.* (25) reported a 1.23–1.46 gain at 3 T using a standard head coil. In the present study, parallel imaging was applied for both 3 T and 1.5 T DTI in order to reduce geometric distortion and acquisition time. Parallel imaging is essential to modern DTI (26,27) and may be attributable to higher SNR gain, including the posterior fossa and basal ganglia, compared with previous studies. In experimental studies, FA is sensitive to low SNR, because the value that is sensitive to isotropic diffusion, such as in cerebrospinal fluid, erroneously shows relatively high anisotropy in low SNR images (28,29). Conversely, MD is less sensitive to low SNR, as MD always underestimates true diffusion anisotropy (28).

Parallel imaging is an up-to-date technique and essential in DTI, especially at high-field magnetization, as it can reduce geometric distortion and susceptibility effects by shortening the echo train of the echo planar sequence (26,27). Furthermore, parallel imaging enables DTI with higher spatial resolution by reducing the echo train. We applied the same algorithm of parallel imaging to both 3 T and 1.5 T DTI and compared whole-brain histogram analyses at both magnets among many subjects, which has not been previously reported.

Determining differences in FA and MD under different magnetic fields is necessary, as DTI is performed at many institutes using various settings. The results of histogram and ROI analyses in this study add to our understanding of different magnets. Particularly when studying subtle changes in FA and MD, the use of MR machines of identical magnetic field strength is important.

We focused on FA and MD in this study as these two scalars are commonly used in clinical studies. They are rotationally invariant and appropriate for comparison among individuals because FA represents anisotropy of the diffusion tensor ellipsoid and MD is an orientationally averaged value of the diffusion tensor (30). On the other hand, the first eigenvector with the largest eigenvalue is assumed to represent the local fiber direction and is used for fiber tractography (20,21). However, there might be large differences in the first eigenvector among individuals, as it represents only one direction of the ellipsoid and it is not truly rotationally invariant.

CONCLUSION

In conclusion, this study shows differences in FA and MD at 3 T and 1.5 T with whole-brain histogram and ROI analysis. DTI with parallel imaging at 3 T showed higher FA values than at 1.5 T in ROI analysis. Mean FA at 3 T was higher than at 1.5 T, and peak location at 3 T was lower than at 1.5 T in histogram analysis, which means anisotropic tissue such as white matter shows higher FA values at 3 T than at 1.5 T. Significant differences in FA and MD were shown at 3 T and 1.5 T in this study, which was different from the previous study (17). The SNR increase resulting from the use of parallel imaging and reduction in geometric distortion especially at 3 T may be the reasons. Furthermore, our data are supported by whole-brain analysis of a relatively large population, which was also different from the previous study (17). The SNR of DTI at 3 T increased with parallel imaging. Jaermann *et al.* (27) reported improved resolution at 3 T by using parallel imaging, which is due to the higher SNR and fewer susceptibility artifacts. However, there is no comparison study of DTI with parallel imaging at both 3 T and 1.5 T. We have revealed higher SNR in DTI using parallel imaging at 3 T than at 1.5 T.

Acknowledgement

This study was supported in part by a Japanese Health and Labour Sciences Research Grant (H15-003).

REFERENCES

1. Basser PJ, Mattiello J, LeBihan D. MR diffusion tensor spectroscopy and imaging. *Biophys J.* 1994; 66: 259–267.
2. Beaulieu C. The basis of anisotropic water diffusion in the nervous system: a technical review. *NMR Biomed.* 2002; 15: 435–455.

Copyright © 2007 John Wiley & Sons, Ltd.

3. Chenevert TL, Brunberg JA, Pipe JG. Anisotropic diffusion in human white matter: demonstration with MR techniques in vivo. *Radiology* 1990; **177**: 401–405.
4. Pierpaoli C, Jezzard P, Basser PJ, Barnett A, Di Chiro G. Diffusion tensor MR imaging of the human brain. *Radiology* 1996; **201**: 637–648.
5. Sakuma H, Nomura Y, Takeda K, Tagami T, Nakagawa T, Tamagawa Y, Ishii Y, Tsukamoto T. Adult and neonatal human brain: diffusional anisotropy and myelination with diffusion-weighted MR imaging. *Radiology* 1991; **180**: 229–233.
6. Basser PJ, Pierpaoli C. Microstructural and physiological features of tissues elucidated by quantitative-diffusion-tensor MRI. *J. Magn. Reson. B* 1996; **111**: 209–219.
7. Filippi M, Cercignani M, Inglese M, Horsfield MA, Comi G. Diffusion tensor magnetic resonance imaging in multiple sclerosis. *Neurology* 2001; **56**: 304–311.
8. Bammer R, Augustin M, Strasser-Fuchs S, Seifert T, Kapeller P, Stollberger R, Ebner F, Hartung HP, Fazekas F. Magnetic resonance diffusion tensor imaging for characterizing diffuse and focal white matter abnormalities in multiple sclerosis. *Magn. Reson. Med.* 2000; **44**: 583–591.
9. Werring DJ, Clark CA, Barker GJ, Thompson AJ, Miller DH. Diffusion tensor imaging of lesions and normal-appearing white matter in multiple sclerosis. *Neurology* 1999; **52**: 1626–1632.
10. Bozzali M, Franceschi M, Falini A, Pontesilli S, Cercignani M, Magnani G, Scotti G, Comi G, Filippi M. Quantification of tissue damage in AD using diffusion tensor and magnetization transfer MRI. *Neurology* 2001; **57**: 1135–1137.
11. Muller MJ, Greverus D, Dellani PR, Weibrich C, Wille PR, Scheurich A, Stoeter P, Fellgiebel A. Functional implications of hippocampal volume and diffusivity in mild cognitive impairment. *Neuroimage* 2005; **28**: 1033–1042.
12. Ellis CM, Simmons A, Jones DK, Bland J, Dawson JM, Horsfield MA, Williams SC, Leigh PN. Diffusion tensor MRI assesses corticospinal tract damage in ALS. *Neurology* 1999; **53**: 1051–1058.
13. Sach M, Winkler G, Glauche V, Liepert J, Heimbach B, Koch MA, Buchel C, Weiller C. Diffusion tensor MRI of early upper motor neuron involvement in amyotrophic lateral sclerosis. *Brain* 2004; **127**: 340–350.
14. Nusbaum AO, Tang CY, Wei T, Buchsbaum MS, Atlas SW. Whole-brain diffusion MR histograms differ between MS subtypes. *Neurology* 2000; **54**: 1421–1427.
15. Cercignani M, Iannucci G, Rocca MA, Comi G, Horsfield MA, Filippi M. Pathologic damage in MS assessed by diffusion-weighted and magnetization transfer MRI. *Neurology* 2000; **54**: 1139–1144.
16. Cercignani M, Inglese M, Pagani E, Comi G, Filippi M. Mean diffusivity and fractional anisotropy histograms of patients with multiple sclerosis. *AJNR Am. J. Neuroradiol.* 2001; **22**: 952–958.
17. Hunsche S, Moseley ME, Stoeter P, Hedehus M. Diffusion-tensor MR imaging at 1.5 and 3.0 T: initial observations. *Radiology* 2001; **221**: 550–556.
18. Okada T, Miki Y, Fushimi Y, Hanakawa T, Kanagaki M, Yamamoto A, Urayama S, Fukuyama H, Hiraoka M, Togashi K. Diffusion-tensor fiber tractography: intraindividual comparison of 3.0-T and 1.5-T MR imaging. *Radiology* 2006; **238**: 668–678.
19. Sodickson DK, Manning WJ. Simultaneous acquisition of spatial harmonics (SMASH): fast imaging with radiofrequency coil arrays. *Magn. Reson. Med.* 1997; **38**: 591–603.
20. Mori S, van Zijl PC. Fiber tracking: principles and strategies: a technical review. *NMR Biomed.* 2002; **15**: 468–480.
21. Mori S, Frederiksen K, van Zijl PC, Stieltjes B, Kraut MA, Solaiyappan M, Pomper MG. Brain white matter anatomy of tumor patients evaluated with diffusion tensor imaging. *Ann. Neurol.* 2002; **51**: 377–380.
22. Edelstein WA, Bottomley PA, Pfeifer LM. A signal-to-noise calibration procedure for NMR imaging systems. *Med. Phys.* 1984; **11**: 180–185.
23. Cercignani M, Bammer R, Sormani MP, Fazekas F, Filippi M. Inter-sequence and inter-imaging unit variability of diffusion tensor MR imaging histogram-derived metrics of the brain in healthy volunteers. *AJNR Am. J. Neuroradiol.* 2003; **24**: 638–643.
24. Papanikolaou N, Karampekios S, Papadaki E, Malamas M, Maris T, Gourtsoyiannis N. Fractional anisotropy and mean diffusivity measurements on normal human brain: comparison between low- and high-resolution diffusion tensor imaging sequences. *Eur. Radiol.* 2006; **16**: 187–192.
25. Gonen O, Gruber S, Li BS, Mlynarik V, Moser E. Multivoxel 3D proton spectroscopy in the brain at 1.5 versus 3.0 T: signal-to-noise ratio and resolution comparison. *AJNR Am. J. Neuroradiol.* 2001; **22**: 1727–1731.
26. van den Brink JS, Watanabe Y, Kuhl CK, Chung T, Muthupillai R, Van Cauteren M, Yamada K, Dymarkowski S, Bogaert J, Maki JH, Matos C, Casselman JW, Hoogeveen RM. Implications of SENSE MR in routine clinical practice. *Eur. J. Radiol.* 2003; **46**: 3–27.
27. Jaermann T, Crelier G, Pruessmann KP, Golay X, Netsch T, van Muiswinkel AM, Mori S, van Zijl PC, Valavanis A, Kollias S, Boesiger P. SENSE-DTI at 3 T. *Magn. Reson. Med.* 2004; **51**: 230–236.
28. Bastin ME, Armitage PA, Marshall I. A theoretical study of the effect of experimental noise on the measurement of anisotropy in diffusion imaging. *Magn. Reson. Imaging* 1998; **16**: 773–785.
29. Armitage PA, Bastin ME. Selecting an appropriate anisotropy index for displaying diffusion tensor imaging data with improved contrast and sensitivity. *Magn. Reson. Med.* 2000; **44**: 117–121.
30. Basser PJ, Jones DK. Diffusion-tensor MRI: theory, experimental design and data analysis: a technical review. *NMR Biomed.* 2002; **15**: 456–467.

Copyright © 2007 John Wiley & Sons, Ltd.

Validation of anatomical standardization of FDG PET images of normal brain: comparison of SPM and NEUROSTAT

Kayo Hosaka[1], Kazunari Ishii[1, 2], Setsu Sakamoto[3], Norihiro Sadato[4], Hiroshi Fukuda[5], Takashi Kato[6], Kazuro Sugimura[1], Michio Senda[3]

[1] Department of Radiology, Kobe University, Kobe, Japan
[2] Department of Radiology and Nuclear Medicine, Hyogo Brain and Heart Center, Himeji, Hyogo, Japan
[3] Department of Image-Based Medicine, Institute of Biomedical Research and Innovation, Kobe, Japan
[4] Division of Medical Imaging, Biomedical Imaging Research Center, Fukui, Japan
[5] Department of Nuclear Medicine and Radiology, Institute of Development, Aging and Cancer, Tohoku University, Sendai, Japan
[6] Department of Biofunctional Research, National Institute for Longevity Sciences, Obu, Japan

Received: 2 February 2004 / Accepted: 13 April 2004 / Published online: 21 August 2004
© Springer-Verlag 2004

Abstract. *Purpose:* Statistical parametric mapping (SPM) and NEUROSTAT (NS) are widely used for intersubject statistical analysis of brain images. We investigated individual anatomical variations after standardization of ^{18}F-fluorodeoxyglucose positron emission tomography (FDG PET) images of normal brain and compared the differences in the standardized images obtained from SPM and NS.
Methods: Twenty healthy normal subjects were recruited for FDG PET and magnetic resonance imaging (MRI) studies. Sylvian fissures (SF), cingulate sulci (CingS) and central sulci (CtlS) were marked on the brain surface of each individual's co-registered MR images. Then spatial standardization was performed on each subject's PET images using SPM99 and NS with NS's FDG template image, and each subject's MR images (with the SF, CingS, and CtlS marked in advance) were standardized using the sets of parameters obtained from PET standardization by SPM and NS, respectively. The coordinates of each subject's SF, CingS, and CtlS detected on the MR images standardized by the two methods were measured and compared with those on the template images.
Results: The mean individual deviations from the averaged coordinates for the markers on the SF, CingS and CtlS standardized by SPM and by NS were no more than 0.21–1.15 mm. The number of voxels within the brain volume on standardized MR images of all 20 subjects was 88.0% of the total number of brain volume voxels for SPM and 85.3% for NS.
Conclusion: This study demonstrates that SPM and NS yield relatively small differences in standardization and that both methods are effective and valid for PET studies in normal subjects.

Eur J Nucl Med Mol Imaging (2005) 32:92–97
DOI 10.1007/s00259-004-1576-z

Kazunari Ishii (✉)
Department of Radiology and Nuclear Medicine,
Hyogo Brain and Heart Center, 520 Saisho-Ko, Himeji,
Hyogo, 670-0981, Japan
e-mail: ishii@hiabcd.go.jp
Tel.: +81-792-933131, Fax: +81-792-958199

Introduction

A method of anatomical standardization, also called spatial standardization, is commonly used by investigators to compare brain positron emission tomography (PET) images of different subjects voxel by voxel and for intersubject statistical analyses. Although it may seem preferable to obtain morphological information from magnetic resonance (MR) imaging, most investigators standardize PET images by using a software package such as statistical parametric mapping (SPM, The Wellcome Department of Neurology, London, UK) [1] or NEUROSTAT (Department of Internal Medicine, University of Michigan, Ann Arbor, MI, USA) [2], rather than using co-registered MR images such as the human brain atlas (HBA, Department of Neuroscience, Karolinska Institute, Sweden) [3]. This is due to the smaller intersubject variation of voxel values and the lower costs when using PET-based standardization compared with MR-based standardization [4]. However, standardization of PET images without the use of co-registered MR images does not guarantee the anatomical correspondence of standardized images. Sugiura et al. [5] examined the anatomical precision of spatial standardization in the localization of the major sulci and brain contours of $H_2{}^{15}O$ cerebral blood flow images with HBA using MR imaging and compared it with SPM95, without use of MR imaging. Their results showed that, despite the lack of use of MR imaging, SPM95 allowed a similar level of precision as HBA, ex-

cept in a few cases where morphological localization varied greatly from that of other subjects.

Recently, spatial standardization of PET images has been used not only in research but also in clinical diagnoses. Minoshima et al. investigated the clinical usefulness of three-dimensional stereotactic surface projections (3D-SSP), in NEUROSTAT [6]. However, there have been no reports on the accuracy of standardization using morphological landmarks of standardized MR images that are transformed with the same parameters as PET images in normal brain. In addition, there have been no reports on the variations in anatomical landmarks of standardized FDG PET images of the normal brain using FDG templates by SPM.

The purpose of this study, therefore, was to assess the morphological accuracy of two commonly used techniques, SPM and NEUROSTAT, in the anatomical standardization of normal brains, by identifying the location of Sylvian fissures, cingulate sulci and central sulci on co-registered MR images.

Materials and methods

Subjects

Twenty healthy normal subjects (19 males, one female; mean age 38.1±18.9 years, range 18–68 years) were recruited for FDG PET and high-resolution T1-weighted MRI studies. Ten (all males, aged 20.5±3.1 years) were recruited from the Institute of Development, Aging and Cancer (IDAC), Tohoku University, Sendai, Miyagi, Japan and ten (nine males and one female, 55.7±7.5 years) from the National Institute for Longevity Sciences (NILS), Obu, Aichi, Japan.

PET studies

All subjects fasted for at least 6 h before the PET study. Subjects were studied in the resting condition with the eyes blindfolded and ears unplugged in a dimly lit room with minimal noise. An intravenous catheter was inserted in the left antecubital vein and maintained with saline flushing, and 370 MBq of ^{18}F-fluorodeoxyglucose (FDG) was injected. A whole-body PET scanner (SET-2400W, Shimadzu Corporation, Kyoto, Japan) was used at IDAC, with a 20-cm axial field of view, and with acquisition of 63 slices. In-plane spatial resolution was 3.9 mm full-width at half-maximum (FWHM) at the center of the field of view, 4.4 mm FWHM tangentially, and 5.4 mm FWHM radially at 10 cm from the center of the field of view [7]. A two-dimensional data acquisition mode was used, and data acquisition was started 30 s after tracer injection and lasted for 45 min. Images were reconstructed by filtered backprojection with a Butterworth-Ramp filter (cut-off 8 mm, order 2), resulting in an in-plane and an axial resolution of 6.0–6.5 mm FWHM. At NILS, an ECAT EXACT HR47 PET scanner (CTI/Siemens, Knoxville, TN, USA) yielding 47 simultaneous planes with an axial FWHM resolution of 4.8 mm and an in-plane resolution of 3.9×3.9 mm^2 was employed. A two-dimensional data acquisition mode was used, with data acquired from 36 to 60 min after injection. Images were reconstructed by filtered backprojection with a Hanning filter (cut-off frequency at 0.5 cycles/projection element), resulting in an in-plane and an axial resolution of 6.0–6.5 mm FWHM.

MRI studies

For anatomical standardization of PET images, structural MR images for each subject were used. At IDAC, MRI scanning was performed using a Vectra Fast, 0.5-T scanner (GE Yokogawa Medical Systems, Tokyo, Japan) on a separate occasion from, but in close temporal proximity to, the PET study. A regular head coil and conventional T1-weighted, spoiled GRASS (TR 50 ms, TE 12 ms, flip angle 45°, NEX 1, image matrix 160×160) in 3D acquisition mode were used. The voxel size in the final MR image was 0.96×0.96×1.50 mm (x, y and z directions, respectively). At NILS, MRI was performed using a Visart 1.5-T scanner (Toshiba Medical, Tokyo, Japan). The scanning sequence was TR 20 ms, TE 7 ms, flip angle 35°. The voxel size was 0.89×0.89×1.3 mm^3, and the slice gap, 0 mm. The voxels of the obtained MR images were then transformed into a voxel size of 0.89×0.89×0.89 mm^3.

Data analysis

All PET and MR images were transferred to a workstation and image sets were converted to ANALYZE format. We co-registered both PET and MR images for each individual subject using SPM99 and then we removed the extracranial soft tissue from the MR images so the brain surface could be identified by image analysis software (Dr View 5.2; AJS, Tokyo, Japan). Following this, Sylvian fissures, central sulci and cingulate sulci were carefully marked on the brain surface of each subject's MR images on every slice where they were identified by one neuroradiologist referencing the Talairach and Tournoux atlas [8]. Because these sulci are major sulci of the brain and are easy to detect, they have been chosen as landmarks in the previous literature [5].

Anatomical standardization of PET image sets was performed using a program "stereo," which is a part of the program set NEUROSTAT, and a SPM99 normalization program using NEUROSTAT's FDG template image. For SPM anatomical standardization, the number of nonlinear basis functions was set to 7×8×7, the number of iterations to 12 and nonlinear regularization to medium. These default parameters were suggested by SPM. When using a NEUROSTAT template, the bounding box was set to −141.75:145.25, −157.5:129.50, −60.75:73.25; the voxel size was 2.25×2.25×2.25 mm^3, the image size was 128×128×60 and the origin was at (64, 71, 28) [9]. For NEUROSTAT, a total of nine affine transformation parameters were estimated.

Next, we standardized each subject's MR images, on which Sylvian fissures, central sulci and cingulate sulci had been marked in advance, using each parameter obtained from PET standardization by SPM and NEUROSTAT, respectively (Fig. 1). After this procedure, we evaluated the mean individual deviations from the averaged coordinates for each marker on specified planes: Sylvian fissures and cingulate sulci on the resliced coronal plane, central sulci on the axial plane (Fig. 2).

After standardization of the PET image with SPM and NEUROSTAT, the co-registered MRI images without landmarks were standardized with each parameter obtained during the standardization of each PET image. Then the standardized MR images were transformed into binary images inside/outside the brain volume.

Table 1. Mean distance from the center of traced points in applicable slices

	rt. SF	lt. SF	rt. CngS	lt. CngS	rt. CtlS	lt. CtlS
NEUROSTAT	3.65 (2.45–5.05)	3.83 (3.14–4.52)	3.98 (2.66–5.13)	3.34 (2.73–6.10)	5.04 (4.25–5.69)	4.97 (3.61–6.14)
SPM	3.44 (2.92–5.06)	3.2 (2.74–3.64)	3.34 (2.18–5.38)	2.96 (2.18–3.71)	4.12 (3.89–4.45)	3.82 (3.30–4.68)
Mean difference between NEUROSTAT and SPM	0.21	0.63	0.61	0.38	0.92	1.15

Units are mm; the range of individual distances from the center of traced points is shown within parentheses
rt., Right; lt., left; SF, Sylvian fissure; CngS, cingulate sulcus; CtlS, central sulcus

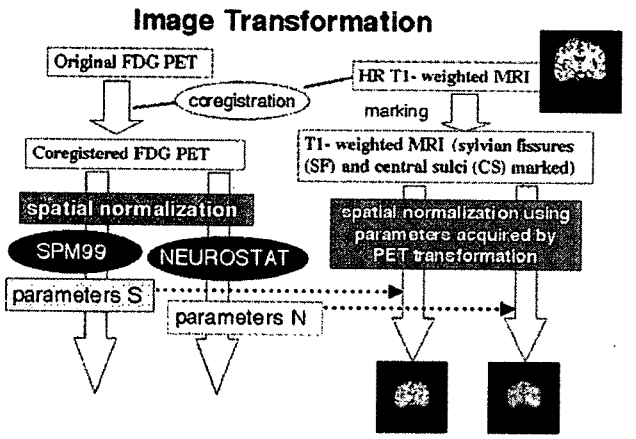

Fig. 1. Process of image transformation in this study. Note that MRI was not used in the process of anatomical standardization but was used for anatomical evaluation. *Parameters S*, image transformation parameters obtained by SPM anatomical standardization; *parameters N*, image transformation parameters obtained by NEUROSTAT anatomical standardization; *HR*, high resolution

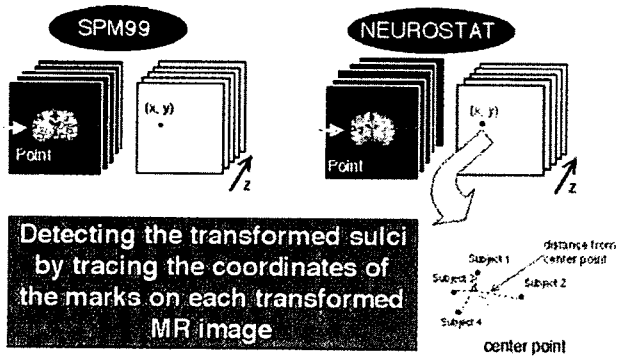

Fig. 2. Definition of center point for each sulcus and definition of each individual distance from the center point on each slice. Center points were defined as the coordinates averaged across subjects

All binary images were summed, and we counted the number of pixels and calculated the overlap ratio; perfect standardization between SPM and NEUROSTAT would result in 100% overlap, and we calculated the ratio in relation to the whole brain area (Fig. 3).

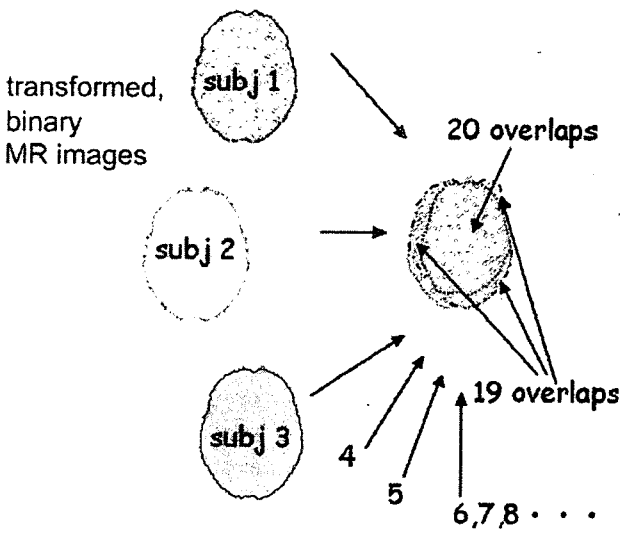

Fig. 3. Method for obtaining the overlap ratio of standardized images of 20 subjects (see text for details)

Results

The mean distance of the subjects' sulcus localization from the center points for each slice in the standardized images differed by no more than 1.15 mm between SPM and NEUROSTAT.

As shown in Table 1, the distance of the Sylvian fissure for each individual subject from the center point ranged from 2.45 mm (on the 62nd slice) to 5.05 mm (on the 68th slice) for NEUROSTAT, and from 2.74 mm (on the 62nd slice) to 5.06 mm (on the 68th slice) for SPM (Fig. 4a). The distance of the cingulate sulci from the center point ranged from 2.66 mm (on the 70th slice) to 6.10 mm (on the 73rd slice) for NEUROSTAT, and from 2.18 mm (on the 73rd slice) to 5.38 mm (on the 53rd slice) for SPM (Fig. 4b). The distance of the central sulci from the center point in the axial slice ranged from 3.61 mm (on the 76th slice) to 6.14 mm (on the 82nd slice) for NEUROSTAT, and from 3.30 mm (on the 80th slice) to 4.68 mm (on the 82nd slice) for SPM (Fig. 4c).

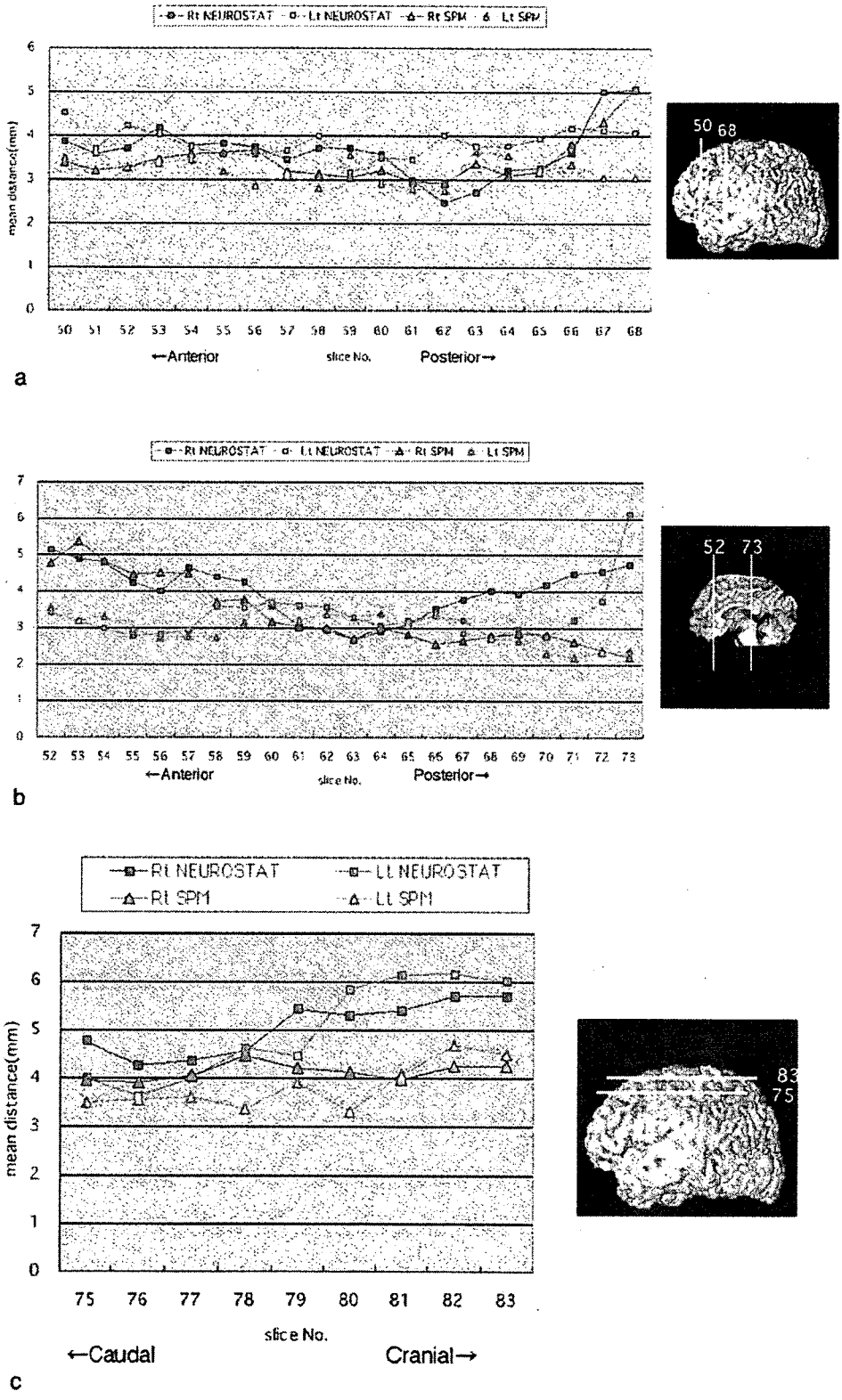

Fig. 4. **a** The mean distance of the subjects' Sylvian fissure localization from the center points for each slice in the standardized images. **b** The mean distance of the subjects' cingulate sulcus localization from the center points for each slice in the standardized images. **c** The mean distance of the subjects' central sulcus localization from the center points for each slice in the standardized images

The 100% overlap ratio of the pixels within the brain volume for the 20 subjects was 83.1% for NEUROSTAT and 84.9% for SPM. The area of the 95% (=19/20) overlap ratio occupied 4.6% with NEUROSTAT and 3.8% with SPM. The area of 70–95% overlap ratio with NEUROSTAT was a little larger than that with SPM (Fig. 5). There was no significant difference in the area of the 20–60% overlap ratio between NEUROSTAT and SPM.

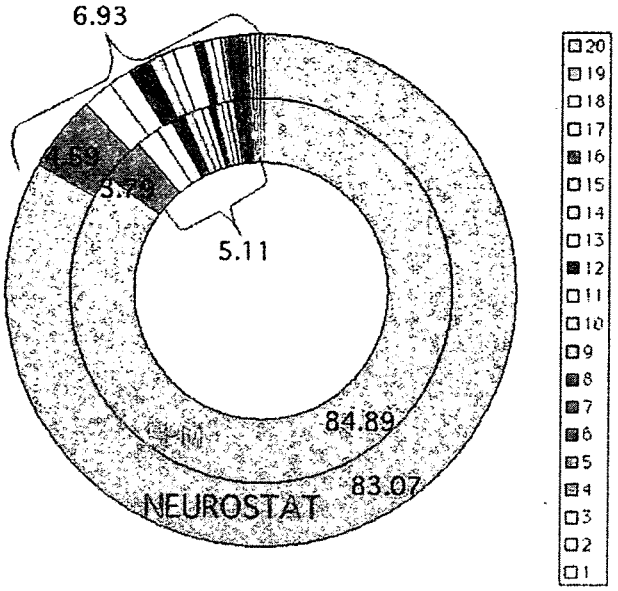

Fig. 5. Percentage of overlap of standardized images for 20 subjects. *The blue area* shows percentage of overlap area for all 20 standardized images

Discussion

In a previous validation of anatomical standardization for atrophied brain that included both healthy volunteers and Alzheimer's disease (AD) patients, the investigators concluded that NEUROSTAT and SPM yielded grossly similar patterns in FDG PET images of AD [9]. In our study we focused only on the brains of healthy volunteers, and we also found no major differences between the standardized FDG PET images with SPM and NEUROSTAT. We examined normal subjects because no study has been done on this topic and because such investigations should first be performed in normal subjects. SPM and NEUROSTAT are expected to be and are actually used for patients, but it is well known that there are some cases where normalization does not work satisfactorily. How the anatomical correspondence matches or varies for patients is an important issue and will be a target of future work.

Many investigators are interested in whether they can find hypometabolic changes in target regions, e.g., hippocampus in AD. The question is, "Which is larger, the size of the hypometabolic area or the degree of the individual variation for the spatial normalization?" We did not examine the variation for the hippocampus in the present study, but found the variation for the central sulcus and cingulate sulcus to be <1 cm on average; this result may be extrapolated to other regions. Because the hypometabolic area in the target regions in focal cortical neurodegenerative disorders is usually sufficiently larger, it will be visualized by either SPM or NEUROSTAT.

In a methodological study, use of a single scanner is usually preferable. The present study, however, used two different scanners because many investigators currently use them together with SPM or NEUROSTAT [5, 9] and we did not want the results to be applicable only to a specific scanner. In fact, there is a trend toward establishing a normal database acquired with a certain scanner, with which patient images acquired with a different scanner will be compared. Because both scanners provide sufficient image quality that allows spatial normalization by SPM or NEUROSTAT and because the most important part of the analysis was done for each subject before summarizing the results in the present study, use of two different scanners is not likely to have affected the results significantly.

In the NEUROSTAT algorithm, differences in brain size between the individual brain and the standard template are removed by linear scaling. Then, to adjust the individual brain shape to the stereotactic atlas proposed by Talairach and Tournoux [8], nonlinear warping along the directions of major neuronal fiber bundles within the brain is performed [2]. This process is the most characteristic feature of the NEUROSTAT algorithm. In contrast, in SPM99 the first step of the standardization is to determine the optimum 12-parameter affine transformation. Next, nonlinear deformation of the individual brain shape is performed by a linear combination of three-dimensional discrete cosine transform basis functions. Matching involves simultaneous minimization of membrane energies from the deformation fields and the residual squared difference between the images and template [10]. In spite of the difference in the algorithm between these two programs, only a small difference in the morphological correspondence was observed in this study. The mean distance from the center point in each fissure was no more than 6.14 mm. While the mean distance from the center point in each fissure standardized by NEUROSTAT was a little larger than that observed with SPM in all six fissures, the difference was no more than 1.15 mm. Considering the resolution of PET images, we believe this will not cause any serious errors.

The mean distance from the center point of the central sulcus was the largest among the three fissures. This may be because the distance between the AC–PC plane and the sulcus is larger than that between the AC–PC plane and the Sylvian fissure or cingulate sulcus. The mean distance from the center point bilaterally of the cingulate sulcus and Sylvian fissure standardized by two different techniques had a similar value in each slice. Therefore, it is supposed that the difference mainly depends on individual variation in the shape of the sulcus rather than on the algorithm of standardization. There is wide variation in individual fissures or sulci even in normal healthy subjects [5, 9]. Therefore, it is natural that variations remain after anatomical standardization.

We supposed that the overlap ratio is one of the indicators of precise anatomical standardization and re-

flects cortical mismatches among the individual standardized images. In programming a study with SPM or NEUROSTAT, before voxel-by-voxel statistics, precise anatomical standardization is needed. If the overlap ratio is small, the voxel-by-voxel statistics will lead to mistakes, especially at the voxels of cortical ribbons.

The complete overlap area of the 20 brains standardized by SPM was slightly larger than that standardized by NEUROSTAT. However, the difference was very small and we expect that this difference will not exceed the variance in individual brain contours. With NEUROSTAT, after anatomical standardization, peak cortical activities are extracted and are projected to surface pixels, and then statistics are performed [8]. This procedure (3D-SSP) has merit in compensating for the small mismatch of cortical regions in anatomical standardization, though SMP performs voxel-by-voxel statistics directly.

Theoretically, NEUROSTAT's anatomical standardization seems superior to SPM's mathematical standardization and it was validated in the study of atrophied brain [9]. However, the results showed that SPM is slightly superior in transforming FDG images to the same anatomical space in the brains of normal subjects. Sugiura's study [5] reported the superiority of SPM 95, which is an old version of SPM 99, compared with HBA, though HBA uses anatomical images while SPM 95 does not. As no perfect standardization technique currently exists, we believe that these two anatomical standardization programs provide acceptable results.

In conclusion, we found that differences in FDG distribution after anatomical standardization with SPM and NEUROSTAT were very small. Both techniques are effective and valid for FDG PET studies in normal subjects.

References

1. Friston KJ, Ashburner J, Frith CD, Poline J-B, Heather JD, Frackowiak RSJ. Spatial registration and normalization of images. Hum Brain Mapp 1995;3:165–189
2. Minoshima S, Koeppe RA, Frey KA, Kuhl DE. Anatomical standardization: linear scaling and nonlinear warping of functional brain images. J Nucl Med 1994;35:1528–1537
3. Roland PE, Graufelds CJ, Wahlin J, et al. Human brain atlas: for high-resolution functional and anatomical mapping. Hum Brain Mapp 1994;1:173–184
4. Senda, M, Ishii K, Oda, K, et al. Influence of ANOVA design and anatomical standardization on the statistical mapping for PET activation. NeuroImage 1998;8:283–301
5. Sugiura M, Kawashima R, Sadato N, et al. Anatomic validation of spatial normalization methods for PET. J Nucl Med 1999;40:317–322
6. Minoshima S, Frey KA, Koeppe RA, Foster NL, Kuhl DE. A diagnostic approach in Alzheimer's disease using three-dimensional stereotactic surface projections of fluorine-18-FDG PET. J Nucl Med 1995;36:1238–1248
7. Fujiwara T, Watanuki S, Yamamoto S, et al. Performance evaluation of a large axial field-of-view PET scanner: SET-2400W. Ann Nucl Med 1997;11:301–313
8. Talairach J, Tournoux P. Co-planar stereotaxic atlas of the human brain. Stuttgart: Thieme, 1988
9. Ishii K, Willoch F, Minoshima S, et al. Statistical brain mapping of ^{18}F-FDG PET in Alzheimer's disease: validation of anatomic standardization for atrophied brains. J Nucl Med 2001;42:548–557
10. Ashburner J, Friston KJ. Nonlinear spatial normalization using basis functions. Hum Brain Mapp 1999;7:254–266

Performance Characteristics of a New 3-Dimensional Continuous-Emission and Spiral-Transmission High-Sensitivity and High-Resolution PET Camera Evaluated with the NEMA NU 2-2001 Standard

Keiichi Matsumoto, MSc[1,2]; Keishi Kitamura, PhD[3]; Tetsuro Mizuta, MSc[3]; Kazumi Tanaka, MSc[3]; Seiichi Yamamoto, PhD[4]; Setsu Sakamoto, MD, PhD[1]; Yuji Nakamoto, MD, PhD[5]; Masaharu Amano, MSc[3]; Kenya Murase, PhD[2]; and Michio Senda, MD, PhD[1]

[1]Department of Image-Based Medicine, Institute of Biomedical Research and Innovation, Kobe, Japan; [2]Division of Medical Technology and Science, Department of Medical Physics and Engineering, Course of Health Science, Graduate School of Medicine, Osaka University, Suita, Japan; [3]R&D Department, Medical Systems Division, Shimadzu Corp., Kyoto, Japan; [4]Department of Electrical Engineering, Kobe City College of Technology, Kobe, Japan; and [5]Department of Diagnostic Imaging and Nuclear Medicine, Kyoto University Graduate School of Medicine, Kyoto, Japan

The SET-3000 G/X (clinical tomograph with high resolution and a large axial field of view) is a 3-dimensional (3D) (only) dedicated PET camera with germanium oxyorthosilicate (GSO) and bismuth germanate (BGO) scintillators. The main characteristic of the SET-3000 G/X PET scanner is 3D continuous-emission and spiral-transmission (CEST) scanning, yielding a reduction in whole-body scan time. We evaluated the physical performance of the SET-3000 G/X PET scanner with the National Electrical Manufacturers Association (NEMA) NU 2-2001 standard. **Methods:** A GSO 3D emission scanner is combined with a BGO transmission scanner separated axially by a lead shield. In the GSO scanner, small and thick scintillators (2.45 × 5.1 × 30 mm^3) are arranged in small blocks (23.1 × 52 mm) to achieve high resolution and a high counting rate. The detector ring has a large solid angle with a diameter of 664 mm and an axial coverage of 260 mm (50 rings). The transmission scanner consists of BGO block detectors with a diameter of 798 mm and an axial width of 23.1 mm and is equipped with a rotating ^{137}Cs point source of 740 MBq and a tungsten collimator. The low- and high-energy thresholds are set to 400 and 700 keV, respectively, in the emission system. The coincidence time window is set to 6 ns. In CEST acquisition, the patient couch moves continuously through the emission and transmission scanners in a 1-way motion. Emission coincidence data are acquired in the histogram mode with on-the-fly Fourier rebinning, and transmission single data are acquired with emission contamination correction. **Results:** With the NEMA NU 2-2001 standard, the main performance results were as follows: the average (radial and tangential) transverse and axial spatial resolutions (full width at half maximum) at 1 cm and at 10 cm off axis were 3.49 and 5.04 mm and 4.48 and 5.40 mm, respectively; the average sensitivity for the 2 radial positions (0 and 10 cm) was 20.71 cps/kBq; the scatter fraction was 50%; the peak noise equivalent count rate was 62.3 kcps at 9.8 kBq/mL; and the peak random rate was 542.1 kcps at 37.6 kBq/mL. **Conclusion:** The new integrated SET-3000 G/X PET scanner has good overall performance, including high resolution and sensitivity, and has the potential of reducing whole-body acquisition time to less than 10 min while improving small-lesion detectability with a low radiation dose.

Key Words: NEMA NU 2-2001; performance test; PET

J Nucl Med 2006; 47:83–90

Early and accurate detection of tumors with ^{18}F-FDG needs a high-performance PET camera that can provide images with high spatial resolution and a high signal-to-noise ratio. In Japan, where cancer screening with ^{18}F-FDG PET of symptom-free subjects is gaining popularity (*1*), PET with a low dose of ^{18}F-FDG and high throughput is desirable. Recently, a new high-resolution and high-sensitivity PET camera (SET-3000 G/X) (*2*) was designed by Shimadzu Corp. and was installed at the Institute of Biomedical Research and Innovation for collaborative performance evaluation and parameter optimization. This PET camera features a new technique called continuous emission and spiral transmission (CEST), which allows high-throughput scanning with transmission-based attenuation correction and the administration of a low radiation dose. In this study, the basic performance of the PET camera was investigated with the National Electrical Manufacturers Association (NEMA)

Received May 23, 2005; revision accepted Sep. 16, 2005.

For correspondence or reprints contact: Keiichi Matsumoto, MSc, Department of Image-Based Medicine, Institute of Biomedical Research and Innovation, 2-2 Minatojima-Minamimachi, Chuo-ku, Kobe 650-0047, Japan.
E-mail: matsumoto@fbri.org

NU 2-2001 standard (*3*) for PET performance measurement. The clinical performance also was tested for a patient with a tumor and was compared with that of the ECAT EXACT HR+ PET camera (Siemens/CTI) (*4,5*).

MATERIALS AND METHODS

Camera Design

The details of the system are described in a previous report (*2*) and are summarized in Table 1. In brief, the PET camera uses cylindrically arranged germanium oxyorthosilicate (GSO) [$Gd_2SiO_5(Ce)$] crystals for dedicated 3-dimensional (3D) emission scanning and a ring of bismuth germanate (BGO) ($Bi_4Ge_3O_{12}$) crystals with a ^{137}Cs point source for transmission scanning; these scanners are coaxially attached and separated by a lead shield for CEST scanning (Fig. 1). The ^{137}Cs point source is collimated axially and transaxially with a tungsten collimator. The rotation speed of the source is 3 s per rotation. Because the point source is highly collimated axially, the background coincidence rate of the emission scanner from the transmission source is considered to be negligible. In fact, the background single rate of the emission scanner from the transmission source is less than 500 cps. Axial collimation also decreases the scatter fraction of the transmission data and provides a more accurate attenuation value. The emission part and the transmission part are separated by a lead shield with a thickness of 32.5 mm to minimize cross contamination. The contamination from the emission detector to the transmission detector is corrected for by masking and measuring the background counts of the off-collimation detectors. Over the clinical range of activity, the attenuation coefficient obtained for a cylindric phantom from transmission data corrected for emission contamination was 0.095 ± 0.02 cm^{-1} (mean ± SD) and was not different from the value for a cold phantom. No significant increase in image noise was observed with this correction method (*2*). This arrangement allows simultaneous emission scanning and transmission scanning with a high-flux transmission source to reduce total scanning time, a goal that is usually difficult when the same detector is used for both purposes. Because there is no transmission source within the emission scanner, the diameter of the emission detector is as small as 664 mm, a feature that increases the solid angle and sensitivity, together with a long axial field of view (FOV) (260 mm). The GSO scintillator enables a small crystal size for high spatial resolution while maintaining scintillating light output. GSO has a high counting rate capability that allows 3D data acquisition with a large solid angle.

TABLE 1
Main Specifications and Characteristics of SET-3000 G/X PET Scanner

Parameter	Emission scanner	Transmission scanner
Detector ring diameter (mm)	664	798
Detector material	GSO	BGO
No. of individual crystals	39,600	2,304
No. of detector blocks	88/ring	48/ring
No. of detector rings	50	6
No. of image planes	99	
Crystal size (mm^3)	2.45 × 5.1 × 30	3.8 × 6.25 × 30
Face of crystal block (mm^2)	23.1 × 52	23.1 × 52
No. of crystals per block	9 × 10	6 × 8
Patient port diameter (mm)	600	600
Axial FOV (mm)	260	23.1
Transaxial FOV (mm)	600	600
Coincidence time window (ns)	6	
Energy window (keV)	400–700	600–800

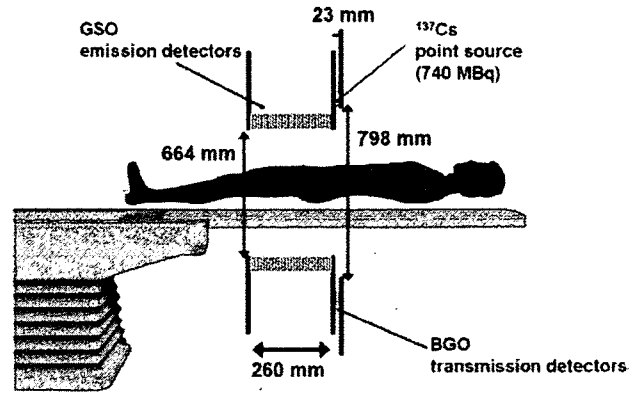

FIGURE 1. Schematic configuration of SET-3000 G/X scanner.

Phantoms

Performance measurements for the SET-3000 G/X scanner were obtained in accordance with the procedure outlined in the NEMA NU 2-2001 standard (*3*). The NEMA NU 2-2001 performance tests require 3 sets of phantoms. The first one is an International Electrotechnical Commission body phantom set, which consists of torso cavity, removable lung insert, and 6 spheres (10–37 mm in inner diameter [ID]). All can be filled. The second one is a scatter phantom set, which includes a solid circular cylinder composed of polyethylene with a specific gravity of 0.96, with an outer diameter of 200 mm, an overall length of 700 mm, and a plastic tube that is 750 mm long and has an ID of 3.2 mm to hold the source activity. The third one is a sensitivity phantom set, which consists of 5 concentric aluminum tubes (each 700 mm long) and a 1.4-mL chloroethylene tube that can be filled and that is inserted into the center sleeve. The NEMA phantoms were manufactured by ITOI Resin Factory Corp. Detailed information and specifications for the NEMA NU 2-2001 phantoms can be found at http://www.itoijyushi.com (in Japanese). As specified by the NEMA NU 2-2001 standard, all measurements were obtained with the ^{18}F isotope.

Performance Measurements

Spatial Resolution. Spatial resolution was measured with a point source of ^{18}F in a glass capillary tube with a 1-mm ID and a 2-mm outer diameter held on foam polystyrene. The axial length was less than 1 mm. The source was positioned at 1 cm and at 10 cm off center of the FOV and at the center and 6.5 cm (one fourth the axial FOV) off center along the axis. More than 100,000 counts were acquired for each source position. Sinograms were rebinned axially with the Fourier rebinning algorithm (*6*); this step was followed by 2-dimensional filtered backprojection (FBP) reconstruction. The full width at half maximum (FWHM) was obtained in the transverse and sagittal images.

Counting Rate and Scatter. The NEMA solid cylindric phantom with a 20-cm diameter and a 70-cm length was made of polyethylene and had a linear hole at 4.5 cm off center. A plastic tube with a 75-cm length and filled with 863.2 MBq of ^{18}F solution was placed in the hole. The phantom was placed at the center of the FOV, and the data were acquired at 90 time points (50 frames of 800 s and 40 frames of 1,600 s) up to 29 h (16 half-lives, to 15.3 kBq, which was 1/56,500 the initial activity). The total count (prompt coincidence) was measured for each frame.

The data were acquired at low counting rates and rebinned with single-slice rebinning (*7*). The sinogram profile was used to calculate the number of scatter events within a diameter of 24 cm (4 cm larger than the phantom diameter) and the number of true events within a 2-cm radius of the source. The scatter within the peak was estimated by assuming a constant background under the peak, the level of which was determined by averaging the intensities near the edge of the peak (at ±2 cm).

The tail-fitting method with a parabolic function was used to estimate the background (scatter plus random) fraction (background counts divided by total counts) for each acquisition frame (*8*). The scatter fraction was estimated at a low counting rate with negligible randoms by use of the procedure recommended in the NEMA NU 2-2001 standard. The true coincidence rate was computed for each frame by subtracting from the prompt coincidence the random plus scatter estimated from the sinograms. The random rate was estimated from the above-described background fraction and the scatter fraction. The noise equivalent count (NEC) rate was computed as (true × true)/prompt coincidence.

Sensitivity. The absolute sensitivity was measured according to the NEMA NU 2-2001 procedure. A 70-cm-long line source with a 3.8-mm ID and filled with 2.3 MBq of ^{18}F solution was scanned with 5 different metal sleeves at the center and 10 cm off center of the FOV. The sensitivity was computed as counts per second per kilobecquerel from the 5 datasets by extrapolating the data to nonattenuation measurements. In the acquisition configuration, the oblique axial coincidence acceptance is up to ±49 planes.

Accuracy of Corrections for Count Losses and Randoms. The accuracy of corrections for dead-time losses and randoms was evaluated. The counting rate measurement was repeated with dead-time correction by use of the cylindric phantom described above; circular regions of interest (ROIs) with an 18-cm diameter were placed on each slice, the measured activity was evaluated against the actual activity concentration of the phantom, and images were reconstructed with FBP.

Image Quality. The NEMA image quality phantom simulating a human torso and containing 6 spheres and a lung insert with a 30-mm-diameter cylinder was used. The background in the phantom was filled with water containing an ^{18}F solution (5.3 kBq/mL). Four of the spheres (10-, 13-, 17-, and 22-mm IDs) were filled with ^{18}F at 4 or 8 times the background activity, and the other 2 spheres (28- and 37-mm IDs) were filled with cold water.

The phantom was positioned at the center, together with the scatter and counting rate phantom containing 116 MBq of ^{18}F simulating activity from outside the target and placed in contact at the edge, and scanned for a 100-cm length for 1 h. The data were corrected for attenuation and scatter and reconstructed with the dynamic row-action maximization-likelihood algorithm (DRAMA) (*9*) with 1 iteration. The scatter correction method used was the convolution subtraction method (*10*). DRAMA is an iterative algorithm similar to the row-action maximization-likelihood algorithm (RAMLA), but the relaxation parameter is controlled in such a way that the noise propagation from projection data to the reconstructed image is independent of the access order of the input data (subsets) in each cycle of the subiterations. An ROI equal to the size of the sphere was placed over each sphere, and the activity was measured. A 30-mm ROI was placed over the lung insert. The hot contrast recovery was computed as [(measured hot/measured background) − 1]/[(actual hot/actual background) − 1], and the cold contrast was computed as 1 − (measured cold/measured background).

The background variability was measured as the SD divided by the mean of a total of 60 ROIs (12 ROIs and 5 slices) placed over the background area, the ROI size being set in 6 different ways to match the sphere sizes. The accuracy of attenuation and scatter correction was computed as the measured lung insert activity divided by the background activity.

Human Imaging

Whole-Body Scan. To evaluate the clinical performance of the SET-3000 G/X scanner, human studies were performed. For the whole-body scan, a patient (height, 172.4 cm; weight, 68.1 kg) with a metastatic tumor mass of unknown origin in the right pelvis and with bone and lymph node metastases was injected with 129.4 MBq of ^{18}F-FDG and was scanned with the SET-3000 G/X camera for 95 cm for 10 min starting 97 min after injection in the CEST mode. For comparison, the same patient was scanned with the ECAT EXACT HR+ scanner for 85 cm for 28 min (2-min emission scan and 2-min transmission scan for each of 7 bed positions) starting 57 min after injection. As the ECAT scanner does not use DRAMA, both images were reconstructed with the ordered-subsets expectation maximization algorithm (*11*) (4 iterations and 8 subsets) after attenuation correction.

Brain Scan. A healthy volunteer (height, 163.4 cm; weight, 56.6 kg) was injected with 183.1 MBq of ^{18}F-FDG and underwent a 10-min emission scan and a 5-min transmission scan in the static mode. The images were reconstructed by use of FBP with a 4-mm gaussian filter after attenuation correction. Image pixel size was 1.0 mm in a 256 × 256 array.

RESULTS

Spatial Resolution

Table 2 shows the spatial resolution of the SET-3000 GX scanner. The spatial resolution was 3.49 mm FWHM at 1 cm off center of the FOV and was degraded to 3.82–5.14 mm FWHM at 10 cm off center. The axial resolutions were 5.04 mm at 1 cm and 5.40 mm at 10 cm off center.

TABLE 2
Measured Spatial Resolution of SET-3000 G/X Scanner

Distance from center (cm)	Direction	FWHM (mm)	FWTM (mm)
1	Transverse	3.49	6.96
1	Axial	5.04	10.60
10	Transverse radial	5.14	7.45
10	Transverse tangential	3.82	9.40
10	Axial	5.40	11.64

FWTM = full width at 10th maximum.

Counting Rate and Scatter

The intrinsic scatter fraction measured at low activity levels was 50%. The peak true counting rate was 224.7 kcps at an activity concentration of 13.7 kBq/mL. The peak NEC rate was 62.3 kcps at 9.8 kBq/mL. The measured counting rates of the trues and randoms and a plot of the NEC rate versus the activity concentration are shown in Figure 2. The random rate reached the true rate at an activity concentration of 7.6 kBq/mL.

Sensitivity

The absolute sensitivities of the SET-3000 G/X scanner were 18.2 cps/kBq with a standard energy window and 23.2 cps/kBq when the line source was placed at the center and at a radial distance of 10 cm. The axial sensitivity profile of the system is shown in Figure 3 for the source at the center of the FOV and at 10 cm off axis.

Accuracy of Corrections for Count Losses and Randoms

Figure 4 shows the relative percent error in measured image activity for the highest, lowest, and average values among the 99 slices that were plotted against the average effective activity concentration. In the NEMA NU 2-2001 standard, bias is defined as the absolute value of the deviation. Over the wide range of the scanner (at the peak NEC rate and below), the maximum bias was less than 11.0%, and the average bias was less than 4.2%.

Image Quality

Table 3 shows the results obtained with the image quality phantom. The measured contrasts of the hot and cold spheres against the background, the average residual attenuation and scatter correction error in the lung region, and background variability are shown. Figure 5 shows images of the image quality phantom at ratios of lesion activity to background activity of 4 and 8.

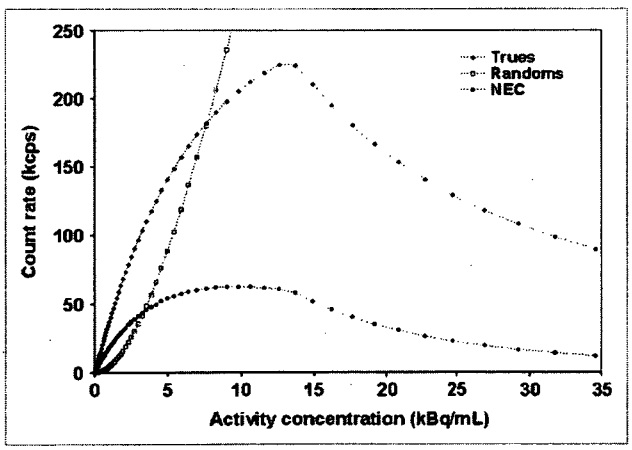

FIGURE 2. Trues, randoms, and NEC rate plotted against activity concentration.

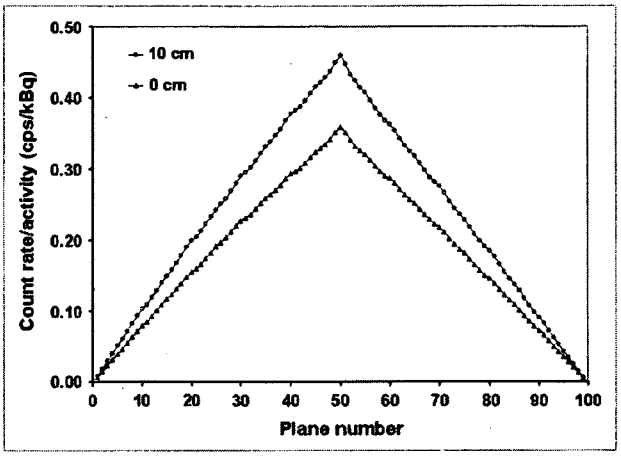

FIGURE 3. Axial sensitivity profile at center of FOV and at 10 cm off center.

Human Imaging

Figure 6 shows the whole-body images obtained for the patient with a tumor by use of the ECAT EXACT HR+ and SET-3000 G/X scanners. Both images revealed high-contrast uptake of ^{18}F-FDG in the pelvic mass, with a complex contour and central necrosis. The bone and lymph node metastases also were demonstrated in both images. The SET-3000 G/X scanner provided images with equivalent diagnostic capability and image quality in one third the scanning time in this study.

Figure 7 illustrates the brain images obtained for the healthy subject; the images revealed fine gray matter structures of the brain.

DISCUSSION

Spatial Resolution

The measured spatial resolution near the center of the FOV was 3.5 mm, a value that is the best of all those that

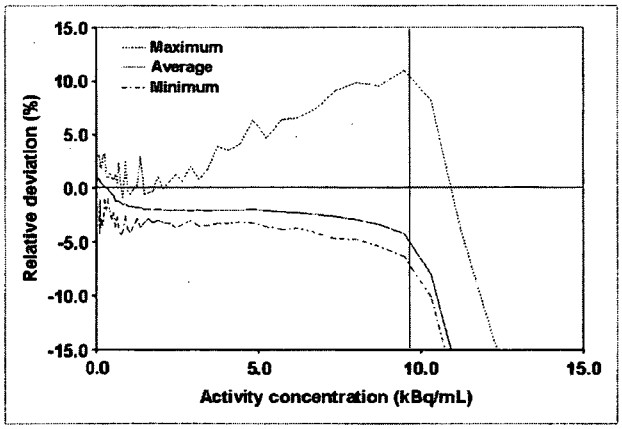

FIGURE 4. Highest and lowest values of relative counting rate error over each slice, in percentages, for each acquisition. Horizontal line indicates 0% bias, and vertical line indicates activity level with peak NEC rate (9.8 kBq/mL). At this activity level, maximum bias was 11.0%.

TABLE 3
Percent Contrast, Background Variability, and Average Lung Residual of SET-3000 G/X Scanner Measured with Image Quality Phantom

Parameter	Sphere diameter (mm)						Lung insert (30 mm)
	10.0	13.0	17.0	22.0	28.0	37.0	
L/B = 4							
Hot-sphere recovery coefficient (%)	17.8	26.3	38.9	65.8			
Cold-sphere contrast (%)					53.2	61.3	
Background variability (%)	11.2	10.9	10.5	9.3	7.5	6.9	
Average residual (%) over lung insert							30.2
L/B = 8							
Hot-sphere recovery coefficient (%)	18.5	27.7	39.0	66.1			
Cold-sphere contrast (%)					50.0	56.8	
Background variability (%)	9.7	9.6	8.4	6.9	6.0	5.7	
Average residual (%) over lung insert							29.3

L/B = ratio of lesion activity to background activity.

have been reported for commercially available whole-body PET cameras for clinical use. This high resolution was realized by reducing the GSO crystal size to 2.45 × 5.1 × 30 mm, and the high light output of GSO enables discrimination of input signals from different crystals. The spatial resolution at 10 cm from the center of the FOV was degraded by 30%, but it was still higher than those of currently available PET cameras (*12–14*). In this work, the spatial resolution was measured at a stationary bed arrangement according to the NEMA NU 2-2001 standard. Similar results were obtained with the CEST data acquisition mode regardless of the bed velocity (3.62 mm FWHM transverse, 5.47 mm FWHM axially at 1 cm off center, 3.93 mm FWHM tangentially, 5.29 mm FWHM radially, and 6.07 mm FWHM axially at 10 cm off center). Therefore, the CEST mode does not degrade spatial resolution.

Counting Rate Characteristics

The scatter fraction was 50%, a value that was somewhat higher than those of currently available PET cameras (*12–14*), possibly because of the large solid angle of this PET camera. The energy window was set to 400–600 keV; this window was narrower than that of BGO cameras because it took advantage of the high light output of the GSO scintillator, but it was wider than that of other GSO cameras to maintain sensitivity. Because the scintillation decay of GSO is 60 ns, far shorter than that of BGO, the coincidence time window was set to 6 ns to reduce the random rate and to maintain the high NEC rate. The measured peak NEC rate (62.3 kcps) was comparable to those of currently available PET cameras but was not as high as that expected from the high sensitivity realized by the 3.0-cm-thick GSO, probably because of the high random rate caused by the large solid angle. The peak NEC rate was observed at an activity concentration of 9.8 kBq/mL, a value that was much higher than that in standard clinical ^{18}F-FDG scans. In the typical clinical situation, in which the body soft-tissue (liver) activity concentration is assumed to be 3 kBq/mL, the NEC rate is 41.1 kcps, a value that is sufficiently high to provide images with high signal-to-noise ratios. However, because it is difficult to match the activity concentration of the NEMA NU 2-2001 phantom to that of the human body, the 70-cm cylinder NEC rate curves may not provide exact predictors of the activity concentrations required for peak NEC rates in whole-body imaging. (*15*).

In any event, the optimum time window and energy window for clinical ^{18}F-FDG whole-body scanning may need further investigation, and the peak NEC rate may be increased.

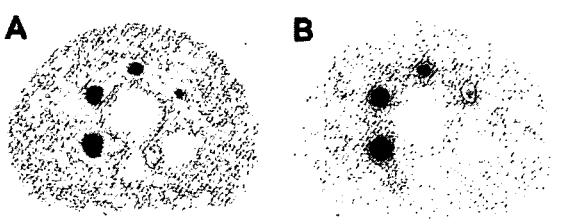

FIGURE 5. Reconstructed images of image quality phantom at ratios of hot-spot lesion activity to background activity of 4 (A) and 8 (B).

Sensitivity

The measured sensitivities (18.2 and 23.2 cps/kBq) were more than twice as high as those of currently available PET cameras (*12–14*). This result was realized by the large solid angle of the detector crystals, with a high packing fraction, and the thick radial crystal size (30 mm). The sensitivity off center of the axial FOV was increased by 30%, possibly because of the small detector diameter. The slice sensitivity was low because of the thin slice. However, the CEST mode allows the use of virtually all lines of response within the detector rings, including those between rings far apart by a maximum of 49 rings, and provides axially

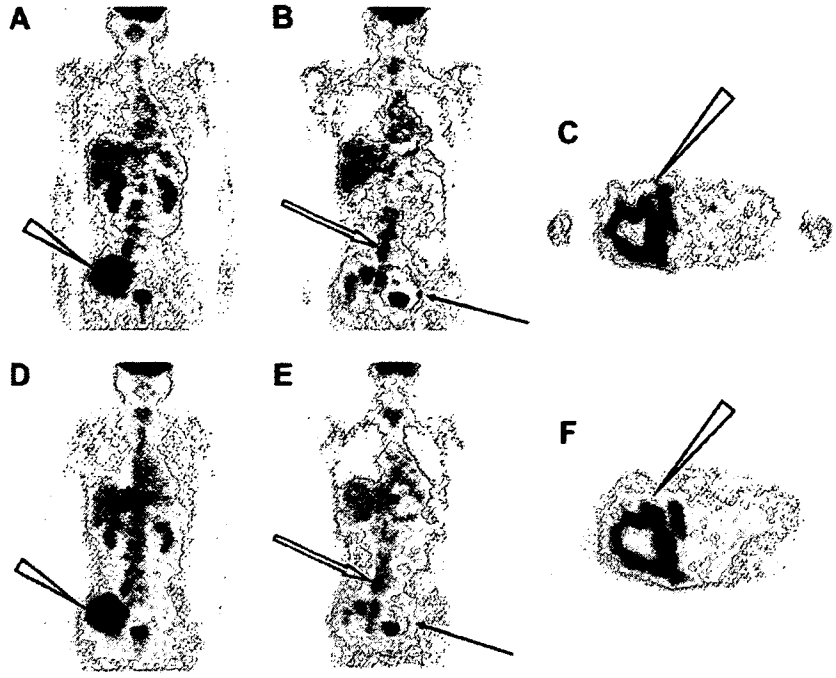

FIGURE 6. PET images obtained with ECAT EXACT HR+ (A–C) and SET-3000 G/X (D–F) scanners. Selected maximum-intensity-projection (A and D), coronal (B and E), and transverse (C and F) slices are shown. Maximum-intensity-projection images show pelvic tumor with high abnormal ^{18}F-FDG uptake (arrowheads). Coronal images show lymph node (solid arrows) and bone (open arrows) metastases. Transverse images show irregular contour and central necrosis of pelvic tumor (arrowheads).

homogeneous sensitivity throughout the length of the scan (*16*).

Accuracy of Corrections for Count Losses and Randoms

The measurement of correction for count losses and randoms shown in Figure 4 indicated consistent negative bias over almost the entire range of activity. This result probably was caused by overestimation and low precision of the reference measurement at the very low activity specified in the NEMA NU 2-2001 protocol, at which a 3D camera may be affected by the environmental background radiation, a situation that is not corrected for in this system. The relative deviation in Figure 4 showed a fairly constant bias of −2.0% to −2.5% in the range of 1–7 kBq/mL, corresponding to the counting rate of the clinical setup. This result suggests that the clinical measurement could be free of significant bias attributable to count losses if calibrated with a phantom with corresponding activity.

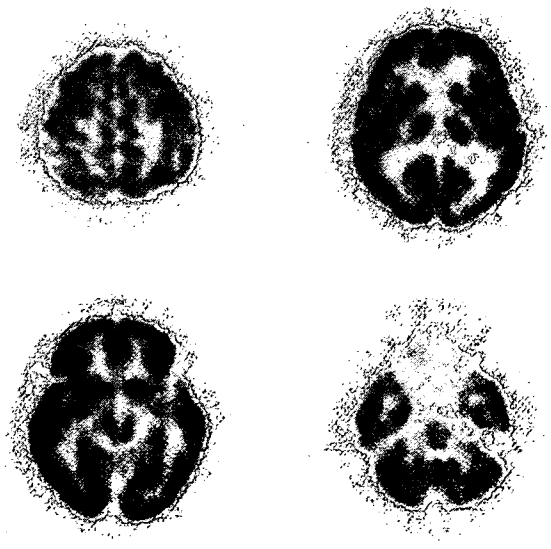

FIGURE 7. Images obtained for healthy volunteer with SET-3000 G/X scanner. Volunteer was scanned 100 min after injection.

Image Quality

The results obtained with the image quality phantom revealed high contrast in hot regions, the measured contrast being higher than those of many other scanners in the 3D mode (*5,12,13*), suggesting a small partial volume attributable to high spatial resolution. This property may increase the detectability of tumors and improve the quantification of ^{18}F-FDG uptake. The measured activities in cold regions and in the lung insert were comparable to the data obtained with other scanners (*5,13*), suggesting that correction for attenuation and scatter was done appropriately.

In general, the PET attenuation correction was done with rotating ^{68}Ge rod sources by coincidence detection or with a ^{137}Cs point source by singles detection, the latter being used in the present PET camera. The singles detection method collects many more counts and provides better statistics than the coincidence detection method, and ^{137}Cs is more economical because it has a much longer half-life (30.2 y) than ^{68}Ge (271 d). As the photons from ^{137}Cs have higher energy (662 keV) than annihilation γ-rays (511 keV), the measured attenuation coefficient is corrected appropriately.

The images were reconstructed with DRAMA (*9*). The noise level determined by visual inspection was low, indicating the effectiveness of this reconstruction algorithm. The measured background variability was higher than those of other scanners despite the higher sensitivity, possibly because the reconstruction parameters for the clinical setup were used. The image noise of RAMLA or DRAMA depends on the reconstruction parameters more than does that of the ordered-subsets expectation maximization algorithm and tends to expand (*5,13,14*). The detailed parameters of DRAMA need to be optimized for routine clinical situations. Additionally, attenuation and scatter correction procedures need to be optimized further.

Human Imaging

The 10-min whole-body ^{18}F-FDG PET scan of a patient with a tumor provided high-quality images visualizing the main tumor with central necrosis as well as bone and lymph node metastases, demonstrating the practicability of the PET camera for oncology scans (Fig. 6). The images were compared with those obtained for the same patient with a 28-min ECAT EXACT HR+ PET scan. Although an exact comparison is impossible because of a change in the radioactivity distribution during the 2 scans, the 2 scans provided equivalent image quality, indicating that the new PET scanner may have patient throughput approximately 3 times higher than that of the ECAT EXACT HR+ scanner for whole-body oncology imaging.

The brain study in Figure 7 revealed high-quality images that clearly visualized the sulci, gyri, and other gray matter structures. These data suggest the possibility and practicability of the use of the new PET scanner for detecting epileptic foci having local hypometabolism as well as for the differential diagnosis of dementia on the basis of the pattern of radioactivity distribution.

Considerations for PET/CT

PET/CT scanners have the great advantage of providing PET/CT fusion images and are rapidly replacing dedicated PET cameras in the market, and the PET camera described in this article can constitute the PET part of a PET/CT scanner. Most of the currently available PET/CT systems use CT for attenuation correction, although CT-based attenuation correction is subject to artifacts attributable to respiratory-phase differences, contrast media, and metals. Furthermore, in those systems, the CT scan must be acquired for the entire axial length of the PET scan to acquire data for attenuation correction and therefore may include areas for which fusion images are not necessarily requested. Because the PET camera described in this article uses the CEST technique, which provides attenuation data without additional scanning time and with little additional radiation exposure, for the transmission scan, CT is not required for attenuation correction if the PET camera is incorporated into a PET/CT system. Instead, with this new PET/CT system, it will be possible to acquire CT not over the entire axial length but only in areas for which fusion images are requested.

The high spatial resolution of the PET scanner will be valuable for the identification of radioactivity uptake from nearby structures, such as lymph nodes versus arterial plaques or bones, even in a PET/CT system. Because of the possible minor mismatch between PET and CT as a result of patient or organ motion, CT does not totally compensate for the spatial resolution of PET, although there is a trend toward disfavoring the spatial resolution of the PET unit in PET/CT systems.

CONCLUSION

The newly designed SET-3000 G/X PET camera uses the CEST technique. The basic performance evaluated with the NEMA NU 2-2001 standard, together with the human images, indicates that it provides high spatial resolution, high sensitivity, and high throughput with a low radiation dose, properties that would be useful and beneficial in a clinical model. It is suitable for whole-body oncology scanning, including cancer screening, as well as brain and heart scanning. This PET camera also can be incorporated into a PET/CT system in which CT may be acquired not over the entire body but only in areas for which fusing images are requested.

ACKNOWLEDGMENTS

We thank Keiji Shimizu, Eiri Minota, Eiji Watanabe, and the cyclotron staff for their expert technical assistance. Part of this study was presented at the European Association of Nuclear Medicine Congress (September 4–8, 2004, Helsinki, Finland).

REFERENCES

1. Yasuda S, Ide M, Fujii H, et al. Application of positron emission tomography imaging to cancer screening. *Br J Cancer.* 2000;83:1607–1611.
2. Kitamura K, Takahashi S, Tanaka A, et al. 3D Continuous emission and spiral transmission scanning for high-throughput whole-body PET. In: Seibert JA, ed. *2004 IEEE Nuclear Science Symposium and Medical Imaging Conference Record.* Rome, Italy: Institute of Electrical and Electronics Engineers, Inc.; 2005:M3-2.
3. National Electrical Manufacturers Association. *NEMA Standards Publication NU 2-2001: Performance Measurement of Positron Emission Tomographs.* Rosslyn, VA: National Electrical Manufacturers Association; 2001.
4. Brix G, Zaers J, Adam LE, et al. Performance evaluation of a whole-body PET scanner using the NEMA protocol. National Electrical Manufacturers Association. *J Nucl Med.* 1997;38:1614–1623.
5. Herzog H, Tellmann L, Hocke C, et al. NEMA-NU2-2001 guided performance evaluation of four Siemens ECAT-PET scanners. *IEEE Trans Nucl Sci.* 2004; 51:2662–2669.
6. Defrise M, Kinahan PE, Townsend DW, et al. Exact and approximate rebinning algorithms for 3-D PET data. *IEEE Trans Med Imaging.* 1997;16:145–158.
7. Daube-Witherspoon ME, Muehllehner G. Treatment of axial data in three-dimensional PET. *J Nucl Med.* 1987;28:1717–1724.
8. Karp JS, Freifelder R, Geagan MJ, et al. Three-dimensional imaging characteristics of the HEAD PENN-PET scanner. *J Nucl Med.* 1997;38:636–643.
9. Tanaka E, Kudo H. Subset-dependent relaxation in block-iterative algorithms for image reconstruction in emission tomography. *Phys Med Biol.* 2003;48: 1405–1422.

10. Bailey DL, Meikle SR. A convolution-subtraction scatter correction method for 3D PET. *Phys Med Biol.* 1994;39:411–424.
11. Hudson HM, Larkin RS. Accelerated image reconstruction using ordered subsets of projection data. *IEEE Trans Med Imaging.* 1994;13:601–609.
12. Surti S, Karp JS. Imaging characteristics of a 3-dimensional GSO whole-body PET camera. *J Nucl Med.* 2004;45:1040–1049.
13. Erdi YE, Nehmeh SA, Mulnix T, et al. PET performance measurements for an LSO-based combined PET/CT scanner using the National Electrical Manufacturers Association NU 2-2001 standard. *J Nucl Med.* 2004;45: 813–821.
14. Mawlawi O, Podoloff DA, Kohlmyer S, et al. Performance characteristics of a newly developed PET/CT scanner using NEMA standards in 2D and 3D modes. *J Nucl Med.* 2004;45:1734–1742.
15. Badawi RD, Adam L-E, Zimmerman RE. A simulation-based assessment of the revised NEMA NU-2 70-cm long test phantom for PET. In: 2001 IEEE Nuclear Science Symposium and Medical Imaging Conference. Piscataway, NJ: IEEE; 2001:M6-6.
16. Kitamura K, Tanaka K, Sato T. Implementation of continuous 3D whole-body PET scanning using on-the-fly Fourier rebinning. *Phys Med Biol.* 2002;47: 2705–2712.

Development of a Flexible End-Shield Using Tungsten Curtains for 3D PET

S. Yamamoto, *Member, IEEE*, S. Sakamoto, K. Matsumoto, and M. Senda, *Member, IEEE*

***Abstract*—In the three-dimensional (3D) acquisition of positron emission tomograph (PET) without septa, random and scatter due to events from outside the field of view (FOV) become a serious problem. They decrease the signal to noise ratio and the quantitation of the image and also limit the count rate capability of the PET system. To reduce these effects, we developed a flexible end-shield using tungsten curtains (curtain-shield) that consists of a mobile stand, a cylindrical support, and flexible tungsten curtains. The tungsten curtains are made of four layers of 30 mm square, 1 mm thick tungsten plates contained in pockets of cloth. Because the tungsten curtains are flexible, they can safely be used even in body studies. Reduction of random and scatter were observed by using the curtain-shield in both phantom and human studies. Results indicate that the curtain-shield has a potential to improve the image quality of PET studies.**

***Index Terms*—End-shield, flexible, positron emission tomography (PET), tungsten.**

I. Introduction

In the three-dimensional (3D) acquisition of positron emission tomograph (PET) without septa, random and scatter due to events from outside the field of view (FOV) become a serious problem. They decrease the signal to noise ratio and the quantitation of images and also limit the count rate capability. One solution to decrease these out-of-FOV events is the use of a fixed end-shield [1]–[3]. However, the shield decreases the diameter of the patient port of the PET scanner and has some difficulties in whole-body studies. Another solution is to use a fixed body-shield [4]–[6]. Although a body-shield can be used for whole body scanning, it needs modifications on the bed. Because the height of the body-shield is shorter than the diameter of the patient port, its use needs more caution to the subject during scanning. To overcome these limitations on fixed-shields, we developed a flexible end-shield using tungsten curtains called curtain-shield.

II. Materials and Methods

In Fig. 1, we show a schematic drawing of a curtain-shield attached to a PET scanner. The curtain-shield consists of a mobile stand, a cylindrical support, and flexible tungsten curtains made of tungsten plates contained in pockets of cloth. They are hung from a cylindrical support. Because the tungsten plates are separated from each others, the curtain-shield is so flexible that subject can be safely moved into or out of the patient port with minimum or no gap between subject and the tungsten curtain.

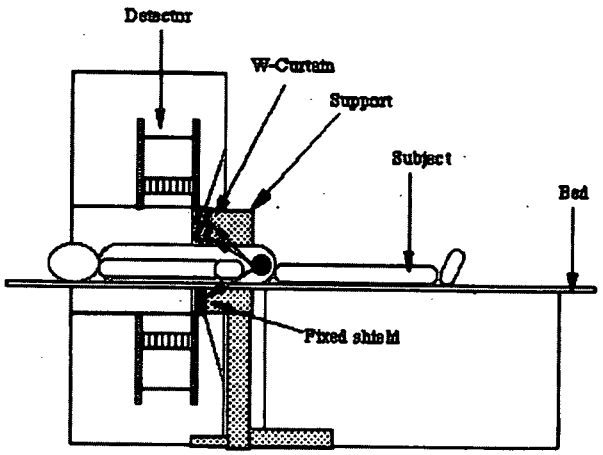

Fig. 1. Schematic drawing of developed shield using tungsten (W) curtains.

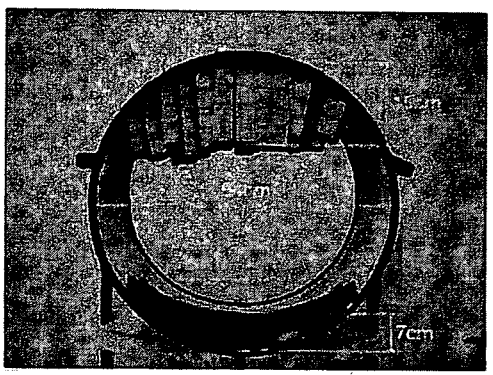

Fig. 2. Photograph of curtain-shield observed from one end of the cylindrical support.

In Fig. 2, we show a photograph of the curtain-shield taken from one end of the cylindrical support. The curtain-shield was designed for CTI EXACT 47 or EXACT HR+ PET scanner. The PET scanner used for the experiments has a ring diameter of 82 cm and patient port of 56 cm. The PET scanner has relatively long (~13 cm) internal fixed end-shields at both sides of the edges of the axial FOV.

The inside diameter of the cylindrical support was 54 cm, slightly smaller than the patient port of the PET scanner. From the upper inside of the cylindrical support, tungsten plates were hung. The size of a single tungsten plate was 30 mm × 30

Manuscript received July 14, 2005; revised March 28, 2006. This work was supported in part by a fund for the Development Program of New Medical Instruments, Kobe City.

S. Yamamoto is with the Kobe City College of Technology, Nishi-ku, Kobe 651-2194, Japan (e-mail: s-yama@kobe-kosen.ac.jp).

S. Sakamoto, K. Matsumoto, and M. Senda are with the Institute of Biomedical Research and Innovation (IBRI), Chuo-ku, Kobe 650-0047, Japan.

Color versions of Figs. 2–6 available online at http://ieeexplore.ieee.org.

Digital Object Identifier 10.1109/TNS.2006.876001

0018-9499/$20.00 © 2006 IEEE

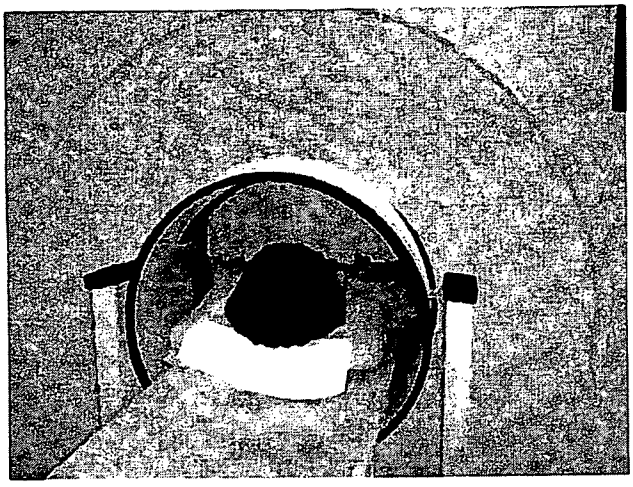

Fig. 3. Photograph of developed curtain-shield with subject.

mm × 1 mm, hung in four layers (4 mm) that absorb approximately 70% of the 511 keV gamma photons. There are some spaces between pockets for the tungsten plates. The maximum length (vertical height) of the curtain-shield was 15 cm.

Also an additional fixed end-shield was inserted in the gap below the bed because this does not disturb patients. The height of the fixed end-shield was 7 cm at maximum, 40 cm wide, and 5 mm thick (4 mm lead plus 1 mm stainless steel). The patient port in the vertical direction was reduced to 32 cm due to the upper and lower shields that may limit the size of the patients. A mobile stand is used to replace the curtain-shield when it is not used.

Fig. 3 shows a developed curtain-shield with a subject. When the curtain-shield touches the subject, it can bend without harming the patient.

III. Results

A. Phantom Experiments

First, we measured the random and scatter rates for a cylindrical phantom positioned out-of-FOV to evaluate the rejection capability of the curtain-shield for these events. A PET scanner, CTI EXACT 47, was used for all of the measurements. The lower energy threshold of the PET scanner was set to 350 keV.

Using a 20 cm diameter, 20 cm height cylindrical phantom that contained 20 MBq of Ge-68, random and scatter rates were measured as a function of the distance between the edge of the axial FOV of the PET scanner and the phantom. The arrangement of the phantom is shown in Fig. 4(A).

Measurements were made with and without the curtain-shield. Because no radioactivity was positioned in the FOV, the prompt minus delay rate measured by PET scanner was identified as scatter rate. An experiment with only a phantom outside the field of view will not necessarily reflect the rejection capability of the shielding for random coincidences since it shows only random coincidences between singles that both arose from activity outside the scanner. Extra random coincidences associated with out-of-FOV activity are, however, more likely between a single from activity within the scanner and a single from activity outside the scanner. The measurement is more a reflection of the reduction of outside singles with the shield.

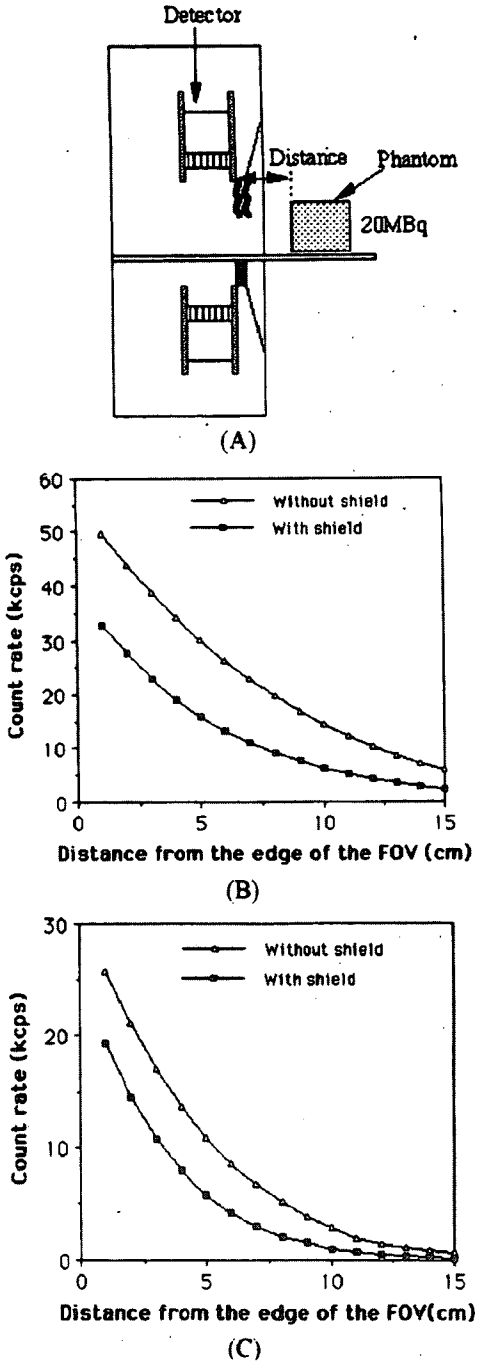

Fig. 4. Experimental set-up for random and scatter rates for phantom positioned out-of-FOV (A), random rate (B), and scatter rate (C) with and without the curtain-shield for a 20 cm diameter, 20 cm height cylindrical phantom positioned out-of-FOV.

Figs. 4(B) and (C) show random and scatter rates as a function of the distance from the edge of the FOV. Using the curtain-shield, random rate decreased 35%–60% and scatter rate decreased 25%–65% depending on the position of the phantom.